

Turbulence Measurements from Compliant Moorings - Part II: Motion

Correction

Levi F. Kilcher*

National Renewable Energy Laboratory, Golden, Colorado, USA

Jim Thomson

Applied Physics Laboratory, University of Washington, Seattle, Washington, USA

Samuel Harding

Pacific Northwest National Laboratory, Richland, Washington, USA

Sven Nylund

Nortek AS, Norway

* *Corresponding author address:* Levi Kilcher, National Renewable Energy Laboratory, 15013 Denver West Pkwy, Golden, Colorado, USA

E-mail: Levi.Kilcher@nrel.gov

ABSTRACT

14 Acoustic Doppler velocimeters (ADV) are a valuable tool for making
15 high-precision measurements of turbulence, and moorings are a convenient
16 and ubiquitous platform for making many kinds of measurements in the
17 ocean. However—because of concerns that mooring motion can contami-
18 nate turbulence measurements and acoustic Doppler profilers are relatively
19 easy to deploy—ADVs are not frequently deployed from moorings. This
20 work demonstrates that inertial motion measurements can be used to reduce
21 motion-contamination from moored ADV velocity measurements. Three dis-
22 tinct mooring platforms were deployed in a tidal channel with inertial-motion-
23 sensor-equipped ADVs. In each case, the motion correction based on the in-
24 ertial measurements dramatically reduced contamination from mooring mo-
25 tion. The spectra from these measurements have a shape that is consistent
26 with other measurements in tidal channels, and have a $f^{-5/3}$ slope at high
27 frequencies—consistent with Kolmogorov’s theory of isotropic turbulence.
28 Motion correction also improves estimates of cross-spectra and Reynold’s
29 stresses. Comparison of turbulence dissipation with flow speed and turbu-
30 lence production indicates a bottom boundary layer production-dissipation
31 balance during ebb and flood that is consistent with the strong tidal forcing
32 at the site. These results indicate that inertial-motion-sensor-equipped ADVs
33 are a valuable new tool for measuring turbulence from moorings.

34 1. Introduction

35 Acoustic Doppler velocimeters (ADV) have been used to make high-precision measurements of
36 water velocity for over 20 years (Kraus et al. 1994; Lohrmann et al. 1995). During that time, they
37 have been deployed around the world to measure turbulence from a range of platforms, including
38 stationary structures on ocean- and lake-bottoms, in surface waters from a pole lowered from
39 a ship’s bow, and in the deep ocean from autonomous underwater vehicles (e.g., Voulgaris and
40 Trowbridge 1998; Zhang et al. 2001; Kim et al. 2000; Goodman et al. 2006; Lorke 2007; Geyer
41 et al. 2008; Cartwright et al. 2009).

42 A relatively small fraction of ADV measurements have been made from moorings (e.g., Fer
43 and Paskyabi 2014). Presumably this is because mooring motion can contaminate ADV mea-
44 surements, and acoustic Doppler profilers (ADPs) can be used to measure mid-depth turbulence
45 statistics without a mooring (e.g., Stacey et al. 1999a; Rippeth et al. 2002; Wiles et al. 2006).
46 Still, ADV measurements have distinct characteristics that can be advantageous: they are capa-
47 ble of higher sample rates, have higher signal-to-noise ratios, and have a much smaller sample
48 volume (1 centimeter, as opposed to several meters). That is, compared to an ADP, ADVs are
49 high-precision instruments capable of providing unique information. They could be more widely
50 used as a moored instrument (i.e., at an arbitrary depth) if a method for accounting for mooring
51 motion can be demonstrated to provide more accurate estimates of turbulence statistics.

52 Inertial motion unit (IMU) sensors have been used in the aerospace and aeronautical industries
53 to quantify the motion of a wide range of systems, and to improve atmospheric velocity measure-
54 ments, for several decades (Axford 1968; Edson et al. 1998; Bevly 2004). Over the last 10 years,
55 the smartphone, drone, and ‘Internet of Things’ markets has driven innovation in microelectrical-
56 mechanical systems, including the IMU. As a result of this growth and innovation the cost, power

57 requirements, and size of IMUs have come down. These changes have allowed these sensors to be
58 integrated into oceanographic instruments that have small form-factors, and rely on battery power.

59 Nortek now offers a version of their Vector ADV with a Microstrain 3DM-GX3-25 IMU sensor
60 (Nortek 2005; MicroStrain 2012). This IMU's signals are incorporated into the Vector data stream
61 so that its motion and orientation signals are tightly synchronized with the ADV's velocity mea-
62 surements. This tight synchronization provides a data stream that can be utilized to quantify ADV
63 motion in the Earth's inertial reference frame, and remove that motion from the ADV's velocity
64 measurements at each time step of its sampling (Edson et al. 1998). This work utilizes moored
65 'ADV-IMU' measurements from mid-depths in Puget Sound to demonstrate that motion correc-
66 tion can improve the accuracy of oceanic turbulence spectra, turbulence dissipation, and Reynolds
67 stress estimates from moored platforms.

68 This effort was originally motivated by a need for low-cost, high-precision turbulence measure-
69 ments for the emerging tidal energy industry (McCaffrey et al. 2015; Alexander and Hamlington
70 2015). Experience in the wind energy industry has shown that wind turbine lifetime is reduced by
71 atmospheric turbulence, and the same is expected to be true for tidal energy turbines. In wind, me-
72 teorological towers are often used to position sonic anemometers at the hub height of wind turbines
73 for measuring detailed turbulence inflow statistics (Hand et al. 2003; Kelley et al. 2005; Mücke
74 et al. 2011; Afgan et al. 2013). In the ocean, tower-mounted hub-height turbulence measurements
75 have been made, but they are challenging to install and maintain in energetic tidal sites (Gunawan
76 et al. 2014; Thomson et al. 2012). Therefore, the U.S. Department of Energy funded this work to
77 investigate the accuracy of mooring-deployed ADV-IMUs to reduce the cost of turbulence mea-
78 surements at tidal energy sites (Kilcher et al. 2016). The approach proved to be successful and
79 potentially useful to the broader oceanographic community interested in moored turbulence mea-

80 surements (Lueck and Huang 1999; Doherty et al. 1999; Nash et al. 2004; Moum and Nash 2009;
81 Alford 2010; Paskyabi and Fer 2013).

82 The next section describes details of the measurements, including a summary of the hardware
83 configurations (platforms) that were used to support and position the ADV-IMUs in the water
84 column. A detailed description of the motion of these platforms is found in the companion paper to
85 this work, Harding et al. (in review), hereafter Part 1. Section 3 describes the mathematical details
86 of motion correction and Section 4 presents results from applying the method to measurements
87 from the various platforms. Section 5 is a discussion of the energetics of the tidal channel in
88 which the measurements were made and demonstrates that the measurements are consistent with
89 turbulence theory and other measurements in similar regimes. A summary and concluding remarks
90 are provided in Section 6.

91 **2. Measurements**

92 This work focuses on measuring turbulence from ADVs that are equipped with IMUs and de-
93 ployed from moving (moored) platforms. The ADVs utilized for these measurements were Nortek
94 Vector ADVs equipped with Microstrain 3DM-GX3-25 IMU sensors. These IMUs captured all
95 six components of the ADV motion (three components of angular rotation and three components
96 of linear acceleration), as well as the orientation of the ADV pressure case. The sampling of the
97 motion sensor is tightly synchronized with the ADV measurements. The IMU measures its mo-
98 tion at 1 kHz and uses internal signal integration (Kalman filtering) to output the motion signals
99 at the same sample rate as the ADV's velocity measurements. This reduces aliasing of the IMU's
100 motion measurements above the ADV's sample rate (MicroStrain 2010). Cable-head ADVs were
101 used throughout this work to allow for flexibility in the positioning of the ADV head relative to its
102 pressure case.

103 All measurements used in this work were made in Admiralty Inlet, Washington, approximately
104 500 m west southwest of Admiralty Head in 60-m of water near 48° 9.18' N, 122° 41.22' W
105 (Figure 1). The site is approximately 6 km east of Port Townsend, and 1 km north of the Port
106 Townsend to Coupeville ferry route. Admiralty inlet is the largest waterway connecting Puget
107 Sound to the Strait of Juan de Fuca, and it possesses a large semidiurnal tidal flow (Thomson
108 et al. 2012; Polagye and Thomson 2013). This work utilizes data from three distinct deployment
109 platforms: the tidal turbulence mooring, a StableMoor buoy, and a simple sounding weight. All
110 data used in this analysis is available from the MHK data repository (<http://mhkdr.openei.org>;
111 submission ids: 49, 50 and 51). Each of these platforms are briefly described below, and additional
112 details, photos, and schematic diagrams can be found in Part 1.

113 *a. Tidal Turbulence Mooring*

114 The tidal turbulence mooring (TTM) is a simple mooring system with a strongback fin sus-
115 pended between a steel clump-weight anchor weighing 1,200 kg when dry and a 0.93-m-diameter
116 spherical steel buoy with a buoyancy of 320 kg. The ADV pressure cases were clamped to one
117 side of the strongback fin and the ADV sensor head was positioned 10 cm in front of the fin's
118 leading edge (Figure 2). The leading edge of the fin is fastened inline with the mooring line. This
119 configuration was designed to work like a weather vane, such that the drag on the fin held the ADV
120 head upstream of the mooring components. This work utilizes data from two TTM deployments.

121 1) JUNE 2012 TTM DEPLOYMENT

122 The first TTM deployment was in June 2012 from 17:30 on the 12th until 14:30 on the 14th
123 (local; i.e., Pacific Daylight Time). Two Nortek ADVs were clamped to either side of the fin so that
124 the axis of their cylindrical pressure cases were parallel with the leading edge of the strongback.

125 The ADV heads were spaced 0.5 m apart vertically along the fin. Only one of these ADVs was
126 equipped with an integrated IMU. This TTM also had an upward-looking acoustic Doppler profiler
127 mounted on the mooring anchor.

128 Periods of time during which this mooring interfered with a beam of the Doppler profiler were
129 identified by inspecting the profiler's acoustic amplitude signal. Periods during which one beam
130 of the profiler had $> 5\%$ higher acoustic amplitude than the other beams were flagged as "contam-
131 inated" and excluded from averaging. Five-minute averages in which more than 50% of the data
132 were contaminated in this way were masked as invalid.

133 2) JUNE 2014 TTM DEPLOYMENT

134 The second TTM deployment was in 2014 from 06:00 on June 17 to 05:00 on June 19 (local
135 time). Two Nortek ADV-IMUs were mounted on this TTM, with their heads spaced 0.5 m apart
136 along the fin. In this case, the pressure cases and ADV heads were inclined at an angle of 18° to
137 the leading edge of the fin to account for mooring blowdown during strong currents (Figure 3).
138 This change was made to reduce vibrational motion observed during the June 2012 deployment
139 that was believed to be associated with the orientation of the pressure cases.

140 *b. The StableMoor platform*

141 The second deployment platform was a cylindrical, StableMoor, syntactic foam buoy (manufac-
142 turer: Deep Water Buoyancy) that was anchored to a clump weight that weighed 2,700 lbs (Figure
143 4). The buoy is 3.5 m long and 0.45 m in diameter with a tail ring that is 0.76 m in diameter. The
144 StableMoor buoy weighs 295 kg in air, and has a buoyancy of 185 kg in water.

145 The StableMoor buoy was deployed with an ADV-IMU mounted at its nose from 11:21 on May
146 12 to 11:53 on May 13, 2015 (local time). The sample volume of the ADV is 10 cm forward of

147 the nose and 20 cm above the center line of the StableMoor buoy (Figure 4). Based on Wyngaard
148 et al.’s (1985) investigation of a similarly shaped slender body, the velocity measurements should
149 have flow-distortion effects of less than 10%. This configuration was designed to be the most
150 stable platform for measuring turbulence from a moving platform. The StableMoor buoy was
151 equipped with a 1,200-kHz RDI workhorse sentinel acoustic Doppler profiler that was oriented
152 downward-looking to measure water velocity below the platform in twelve 1-m bins and measure
153 buoy motion (“bottom tracking”), all at a 1-Hz sample rate.

154 The buoy was ballasted to pitch upward a few degrees in zero-flow to avoid “flying downward.”
155 In the presence of an oncoming current, the tail fins help to orient it into the flow. The anchor for
156 this buoy is similar to that of the TTM, including an acoustic release so the mooring and anchor
157 can be recovered separately.

158 The StableMoor platform has two primary advantages compared to the TTM. First, it is signif-
159 icantly more massive and hydrodynamically stable than the TTM, which reduces the frequency
160 of motions of the platform. Second, the StableMoor platform is capable of supporting a bottom-
161 tracking acoustic Doppler profiler, which provides an independent measure of the platform’s trans-
162 lational motion. Disadvantages of the StableMoor include: its size, which adds to the challenge of
163 deployment and recovery, and its cost, which is significantly higher than the TTM system.

164 *c. Turbulence Torpedo*

165 The turbulence torpedo is a simple sounding weight with an ADV head mounted forward of the
166 nose, and the ADV pressure case strapped below. This platform was deployed on May 14, 2015,
167 for 37 minutes starting at 07:41 local time. This measurement was made from a davit that hung
168 the system from the side of the ship to a depth of approximately 25 m. The primary logistical

advantages of this platform are its compact size, low cost, and the flexibility to perform spatial transects.

d. Coordinate system and turbulence averaging

Unless stated otherwise, vector quantities in this work are in a fixed “principal-axes” coordinate system that is aligned with the bidirectional tidal flow: positive u is in the direction of ebb (310° True), positive w is vertically upward, and v is the cross-stream component in a right-handed coordinate system. The full velocity vector, $\vec{u} = (\tilde{u}, \tilde{v}, \tilde{w})$, is separated into a mean and turbulent component as $\vec{u} = \overline{\vec{u}} + \vec{u}$, where the over-bar denotes a 5-minute average. Turbulence kinetic energy, $\text{tke} = \overline{u^2} + \overline{v^2} + \overline{w^2}$, and Reynold’s stresses, \overline{uv} , \overline{uw} , \overline{vw} , are computed by averaging over the 5-minute window. Throughout this work, we use $\bar{U} = (\bar{u}^2 + \bar{v}^2)^{1/2}$ to denote the mean horizontal velocity magnitude.

All spectra, $S\{x\}(f) = |\mathcal{F}\{x(t)\}|^2$, and cross spectra, $C\{x,y\}(f) = \text{real}(\mathcal{F}\{x(t)\}\mathcal{F}\{y(t)\})$, are computed using NumPy fast Fourier transform routines (van der Walt et al. 2011). Here, $\mathcal{F}\{x(t)\}$ denotes the fast Fourier transform of a signal $x(t)$. Time series, e.g., $x(t)$, are linearly detrended and Hanning windowed prior to computing $\mathcal{F}\{x\}$ to reduce spectral reddening.

Throughout the remainder of this work, the dependence of S and C on f is implied (e.g., $S\{x\}(f)$ is hereafter $S\{x\}$), and for other variables the dependence on t is implied. Spectra and cross spectra are normalized to preserve variance: $\int S\{u\}df = \overline{u^2}$, and $\int C\{u,v\}df = \overline{uv}$. The notations $S\{\vec{u}\} = (S\{u\}, S\{v\}, S\{w\})$, and $C\{\vec{u}\} = (C\{u,v\}, C\{u,w\}, C\{v,w\})$ denote the set of spectra and cross spectra for each velocity component and pairs of components, respectively.

Turbulence dissipation rates are computed as:

$$\varepsilon = \frac{1}{\bar{U}} \left(\alpha \left\langle (S\{u\} + S\{v\} + S\{w\}) f^{5/3} \right\rangle_{fis} \right)^{3/2} \quad (1)$$

Where $\alpha = 0.5$, and $\langle \rangle_{f_{IS}}$ denotes an average over the inertial subrange of the velocity spectra and where the signal-to-noise ratio is small (Lumley and Terray 1983; Sreenivasan 1995). Throughout this work, we take this average from 0.3 to 1 Hz for the u and v components, and 0.3 to 3 Hz for the w component.

3. Methodology

The essential approach of motion correction is to measure velocity on a moving platform and make an independent measurement of the platform motion, then subtract the motion from the velocity measurements. This approach has been used to successfully correct sonic anemometer measurements of atmospheric turbulence (e.g., Edson et al. 1998; Miller et al. 2008). In the ocean, previous works have utilized inertial motion sensors to quantify the motion of multiscale profilers for the purpose of measuring the full spectrum of oceanic shear (Winkel et al. 1996).

Nortek’s ADV-IMU measures the linear acceleration, \vec{a} , rotational motion, $\vec{\omega}$, and orientation matrix, \mathbf{R} , of the ADV pressure case (body) in the Earth reference frame. The Microstrain IMU integrated into the Nortek Vector ADV has been configured to provide estimates of the ADV’s orientation and motion at every time step of the ADV’s sampling (the time synchronization is $O(10^{-2} \text{ s})$). So long as the ADV head is rigidly connected to the IMU (ADV pressure case), the motion of the ADV head is calculated from these signals as the sum of rotational and translational motion:

$$\begin{aligned} \vec{u}_h &= \vec{u}_\omega + \vec{u}_a + \vec{u}_{low} \\ &= \mathbf{R}^T \cdot \vec{\omega}^*(t) \times \vec{\ell}^* + \int \{\vec{a}(t)\}_{HP(f_a)} dt + \vec{u}_{low} \end{aligned} \quad (2)$$

Here, $*$ superscripts denote quantities in the ADV’s local coordinate system, and $\vec{\ell}^*$ is the vector from the IMU to the ADV head. \mathbf{R}^T —the inverse of the orientation matrix—rotates vectors from the IMU to the Earth reference frame. The notation $\{\vec{a}\}_{HP(f_a)}$ indicates that the IMU’s

211 accelerometer signal is high-pass filtered (in the Earth's stationary reference frame) at a chosen
212 filter-frequency, f_a . This is necessary because accelerometers have low-frequency noise, some-
213 times referred to as bias-drift (Barshan and Durrant-Whyte 1995; Bevy 2004; Gulmammadov
214 2009).

215 Integrating \vec{a} to estimate \vec{u}_a amplifies the bias-drift noise at low frequencies, which dramatically
216 reduces the signal-to-noise ratio at those time scales (Figure A1). The high-pass filtering reduces
217 this noise so that it does not contaminate motion correction, but real motion that exists at these
218 frequencies is still lost in the low signal-to-noise ratio (Egeland 2014; VanZwieten et al. 2015).
219 This means that low-frequency motion is not well resolved by the IMU, and so there is a residual
220 low-frequency translational motion, \vec{u}_{low} , that needs to be measured independently—or at the very
221 least considered—when using motion-corrected ADV-IMU data. The $\vec{\omega}$ and \vec{u}_ω estimates do not
222 have the same issue because there is no integration involved, and because low-frequency bias-drift
223 in the $\vec{\omega}$ sensors is stabilized by the IMU's on-board Kalman filtering (i.e., the accelerometer and
224 magnetometer signals provide estimates of down and north, respectively, which stabilize orienta-
225 tion estimates and eliminates bias from rotation estimates).

226 The choice of a high-pass filter for reducing low-frequency accelerometer noise depends on the
227 flow conditions of the measurement and the platform being used. In particular, filter selection in-
228 volves a trade-off between filtering out the bias-drift noise while not filtering out measured motion
229 that is unresolved by an independent measurement of \vec{u}_{low} . Note that, to avoid double counting,
230 \vec{u}_{low} should be estimated by applying the complementary low-pass filter to the independent mea-
231 surement of low-frequency motion.

With this estimate of ADV head motion, it is straightforward to correct the measured velocity, \vec{u}_m , to estimate the velocity in the Earth’s inertial reference frame:

$$\vec{u}(t) = \vec{u}_m(t) + \vec{u}_h(t). \quad (3)$$

Note here that the ‘+’-sign is correct because head motion, \vec{u}_h , induces a measured velocity in the opposite direction of the head motion itself ($\vec{u}_m = \vec{u} - \vec{u}_h$).

For the TTM and turbulence torpedo, we utilize $f_a = 0.0333Hz$ (30-s period) and assume that $\vec{u}_{low} = 0$. For the StableMoor buoy, $f_a = 0.2Hz$ (5-s period). The bottom-track velocity was low-pass filtered at this frequency to provide an estimate of \vec{u}_{low} , and \vec{a} was high-pass filtered at this frequency. We use 4-pole, bidirectional (zero-phase), Hanning filters for all filtering operations.

Additional details on motion correction—including a detailed accounting of the distinct coordinate systems of the IMU, ADV pressure case, and ADV head—can be found in Kilcher et al. (2016). Open-source Python tools for performing motion correction of ADV-IMU data—including scripts that write processed data in Matlab and tabulated formats—are available at <http://lkilcher.github.io/dolfyn/>.

4. Results

a. Mean velocity

Figure 7 shows a comparison of \vec{u} measured by an ADV-IMU mounted on a TTM, to an upward-looking acoustic Doppler profiler mounted on the TTM anchor. This comparison shows excellent agreement between the ADV and Doppler profiler measurements of mean velocity. The \bar{u} , \bar{v} , and \bar{w} components have a root-mean-square error of 0.05, 0.13, and 0.03 m/s, respectively. Although it is important to note that there is some discrepancy between ADP- and ADV-measured velocities (especially in \bar{v} , which is most likely due to incomplete motion correction), the agreement between

the magnitude and direction of these independent velocity measurements indicates that moored ADV-IMUs provide a reliable estimate of mean velocity in the Earth’s reference frame.

b. TTM spectra

As discussed in detail in Part 1, the mooring motion of the TTM, $S\{\vec{u}_h\}$, has a peak at 0.1 to 0.2 Hz from swaying of the mooring that is most likely driven by eddy shedding from the spherical buoy (Figure 8, red lines). There is also higher-frequency broadband motion that is associated with fluttering of the strongback fin around the mooring line. Both of these motions are especially energetic in the v -component spectra because this is the direction in which the TTM mooring system is most unstable. As is expected from fluid-structure interaction theory, the amplitude of these motions increases with increasing mean velocity (Morison et al. 1950).

The mooring motion contaminates the uncorrected ADV measurements of velocity, $S\{\vec{u}_m\}$, whenever the amplitude of the motion is similar to or greater than the amplitude of the turbulence. Fortunately, much of this motion can be removed using the IMU’s motion signals as detailed in Section 3. Lacking an independent measurement of turbulence velocity at this site, we interpret the agreement of these spectra with turbulence theory as evidence that motion correction has improved the velocity measurements. In particular, at high frequencies ($f > 0.3$ Hz) for each mean-flow speed, the spectra decay with a $f^{-5/3}$ slope and have equal amplitude across the velocity components. These results are consistent with Kolmogorov’s (1941) theory of isotropic turbulence, and are consistent with spectral shapes of earlier measurements of turbulence in energetic tidal channels from stationary platforms (Walter et al. 2011; Thomson et al. 2012; McMillan et al. 2016).

For $|\vec{u}| > 1.0$, motion correction modifies the u and v component spectra at frequencies as high as 3 Hz. This outcome indicates that in order for motion correction to be effective, synchronization

276 between the ADV and IMU needs to be within 1/3 s or better. This suggests that asynchronous
277 approaches to motion correction may be challenging, especially considering that the clock drift of
278 some instrumentation can be as high as a few seconds per day. By integrating the IMU data into
279 the ADV data stream, the Nortek ADV-IMU achieves a synchronization to within 1e-2 s.

280 At low frequencies the spectra tend to become roughly constant (especially at higher flow
281 speeds), which is also consistent with previous works. Note that the very low magnitude of $S\{\vec{u}_h\}$
282 at low frequencies is partially a result of filtering the IMU's accelerometer signal when calculating
283 \vec{u}_a . The true low-frequency spectrum of ADV head motion is unknown (indicated using a dashed
284 line below f_a). A comparison of $S\{\vec{u}\}$ measured by the TTM to that measured by the ADP—during
285 the June 2012 deployment—reveals agreement at low frequencies (not shown). This finding sug-
286 gests that the assumption that $\vec{u}_{low} = 0$ at these frequencies and at this site for this platform is
287 justified—even if $S\{\vec{u}_h\}$ is not as low as indicated in Figure 8.

288 As successful as motion correction is, some of the motion contamination persists in $S\{\vec{u}\}$. This
289 is most notable in $S\{v\}$ at the highest flow speeds (> 2.0 m/s): a peak at 0.15 Hz is an order of
290 magnitude larger than a spectral fit to the other frequencies would indicate. This persistent motion
291 contamination is evident to a lesser degree in $S\{u\}$ for $|u| > 2$ m/s, and in $S\{v\}$ at lower flow
292 speeds. $S\{w\}$ appears to have no persistent motion contamination because the amplitude of the
293 motion in this direction is much lower than for the other two components. For these measurements,
294 $S\{w_h\}$ is so low that w -component motion correction makes only a minor correction to the spectra.

295 The amplitude of the persistent motion contamination peaks in $S\{v\}$ at 0.15 Hz is a factor of 5
296 to 10 times smaller than the amplitude of the ADV head motion itself. This observation suggests
297 that the Microstrain IMU can be used to effectively correct mooring motion at 0.15 Hz when
298 the amplitude of that motion is less than 5 times the amplitude of the real turbulence spectrum.

299 As a result, we have chosen a value of 3 as a conservative estimate of the motion correction's
300 effectiveness.

301 In addition to the primary benefit of correcting for mooring motion, the IMU measurements
302 can also be used to identify and screen out persistent motion contamination. For example, one
303 of the most common uses of turbulence spectra is for the calculation of ε and tke . For these
304 purposes, and based on the relative amplitudes of the 0.15-Hz peaks, we assume that persistent
305 motion contamination is likely, where $S\{\vec{u}_h\}/S\{\vec{u}\} > 3$, and thereby exclude these regions from
306 spectral fits.

307 In the present case, for the u and w spectra, this criteria only excludes a narrow range of frequen-
308 cies at the 0.15-Hz motion peak for some cases. This criteria is more restrictive of the v -component
309 spectra at high frequencies for $\bar{U} > 1.0$ m/s, but this may be acceptable because the amplitude of
310 $S\{v\}$ at these frequencies—i.e., in the isotropic inertial subrange—should be equal to that of $S\{u\}$
311 and $S\{w\}$ (Kolmogorov 1941).

312 Agreement of the v -component spectral amplitude with that of u and w at frequencies > 0.3 Hz
313 indicates that motion correction is effective at those frequencies even when $S\{\vec{u}_h\}/S\{\vec{u}\} \gtrsim 3$. This
314 outcome suggests that our screening threshold is excessively conservative at those frequencies,
315 and that a more precise screening threshold may be frequency dependent. For example, it might
316 take into account the f^3 character of the noise in $S\{\vec{u}_a\}$ (Figure A1). For the purpose of this work,
317 the $S\{\vec{u}_h\}/S\{\vec{u}\} < 3$ threshold for spectral fits is sufficient, and detailed characterization of the
318 IMU's motion- and frequency-dependent noise level is left for future work.

319 *c. StableMoor Spectra*

320 The spectra of the StableMoor motion has a broader peak with a maximum amplitude that is ap-
321 proximately half the frequency of the TTM spectral peak (Figure 9). The motion of this platform

also does not have high-frequency “subpeaks” or other high-frequency broadbanded excitation (Part 1). These characteristics of the motion are most likely due to the more massive and hydrodynamically streamlined properties of the platform.

Like the TTM, the motion-corrected spectra from the StableMoor buoy are consistent with turbulence theory and previous observations. Most importantly, there is an improvement in the quality of the motion-corrected spectra compared to the TTM. In particular, the persistent motion contamination peaks are completely removed. That is, this measurement system provides an accurate estimate of the turbulence spectra at this location from low frequencies to more than 1 Hz—well into the inertial subrange—for all three components of velocity.

Note that this level of accuracy cannot be obtained without the independent estimate of \vec{u}_{low} . If we assume that $\vec{u}_{low} = 0$, a similar plot to Figure 9 (not shown) reveals persistent motion-contamination peaks and troughs in the u and v spectra regardless of the choice of f_a . This assumption indicates that the low-frequency motion of the StableMoor buoy is below a threshold in which the IMU’s signal-to-noise ratio is high enough to resolve its motion. In other words, compared to the TTM, the StableMoor platform provides a more accurate measurement of turbulence when it includes an independent measure of \vec{u}_{low} (here a bottom-tracking ADCP), but it does no better—and perhaps worse—when it does not.

d. Torpedo spectra

The u and v motion of the turbulence torpedo is broadbanded and the w motion has a narrow peak at 0.3 Hz (Figure 10). Because \vec{u}_h is estimated using $f_a = 0.0333\text{Hz}$ and assuming $\vec{u}_{low} = 0$, its spectra rolls off quickly below f_a . Motion correction of the torpedo data appears to effectively remove a motion peak from $S\{w\}$ at 0.3 Hz, and straightens out $S\{v\}$ between 0.04 and 0.6 Hz. $S\{u\}$ is mostly unaffected by motion at these frequencies, because the torpedo motion

345 is smaller than the turbulence in this direction. At frequencies below f_a , $S\{u\}$ and $S\{v\}$ increase
 346 dramatically. This increase suggests that unresolved, low-frequency motion of the torpedo is con-
 347 taminating the velocity measurements at these frequencies. It may be possible to correct for some
 348 of this contamination using a measurement of the ship's motion as a proxy for the torpedo's low-
 349 frequency motion, but this has not been done. Still, above f_a , the torpedo appears to provide a
 350 reliable estimate of spectral amplitude in the inertial subrange and can therefore be used to esti-
 351 mate ε . Considering the simplicity of the platform, it may be a useful option for quantifying this
 352 essential turbulence quantity in a variety of scenarios. Further, if a GPS is positioned above it, it
 353 may be capable of providing even more.

354 *e. Cross Spectra*

355 Inspection of cross spectra from TTM measurements demonstrates that motion correction can
 356 reduce motion contamination to produce reliable estimates of velocity cross spectra (Figure 11).
 357 At low flow speeds (left column), cross spectra between components of \vec{u}_h (i.e., between compo-
 358 nents of head motion, red) are small compared to correlated velocities. As the velocity magnitude
 359 increases (center and right columns), the swaying motion of the TTM at 0.15 Hz appears as a peak
 360 in the amplitude of the cross spectra of \vec{u}_h (red) and \vec{u}_m (black) for all three components of cross
 361 spectra (rows). Fortunately, motion correction reduces the amplitude of this peak dramatically so
 362 that $C\{\vec{u}\}$ (blue) is small at 0.15 Hz compared to lower frequencies. Furthermore, the fact that the
 363 standard deviation of $C\{\vec{u}\}$ is also relatively small at 0.15 Hz suggests that motion correction is
 364 effective for each spectral window, not just in their mean.

365 These results indicate that motion-corrected TTM velocity measurements can be used to obtain
 366 reliable estimates of turbulence Reynold's stresses, which are the integral of the cross spectra.

367 Without motion correction, Reynold’s stress estimates would be contaminated by the large peaks
368 in the cross spectra that are caused by the swaying and fluttering motion of the TTM vane.

369 A similar investigation of StableMoor cross spectra (not shown) indicates that cross-spectral
370 motion contamination is at a much lower amplitude than for the TTM. The low-frequency (< 0.3
371 Hz) “swimming” motion of that platform produces a minimal cross-spectral signal, and the relative
372 large mass of the platform minimizes the kinds of higher-frequency swaying and fluttering that
373 creates large values of cross-spectral head motion. Thus, the StableMoor platform also produces
374 reliable estimates of Reynold’s stresses, which are presumed to be improved by motion correction.

375 5. Discussion

376 The previous section presented a comparison of \vec{u} measured by a TTM-mounted ADV to mea-
377 surements from a co-located ADP. This comparison demonstrated that the IMU provides a reliable
378 estimate of the ADV’s orientation and that this can be utilized to estimate mean velocity in the
379 Earth’s reference frame. Turbulence velocity estimates from the same ADP are also in agree-
380 ment with low-frequency TTM turbulence estimates (not shown), but the ADP does not resolve
381 turbulence at the scales where motion contamination is strongest (0.1 to 1.0 Hz).

382 Ideally, moored motion-corrected turbulence velocity measurements would be validated against
383 simultaneous independent validated measurements of turbulence velocity at the same scales and
384 exact time and location. Accomplishing this, however, involves significant technical challenges
385 that are not easily overcome—most notably the difficulty of measuring turbulence at the same point
386 as the moving ADV. A slightly less ideal but much more realistic confirmation of the methodology
387 might involve comparing the statistics of moored turbulence measurements to those from a nearby
388 fixed platform, or a fixed platform placed at the same location at a different time (e.g., the “TTT”

platform described in Thomson et al. 2012). Unfortunately, to our knowledge, these measurements have not yet been made.

Lacking a relevant, fixed, independent turbulence measurement to compare to it is instructive to demonstrate the degree to which the moored measurements are consistent with turbulence theory and other turbulence measurements in similar flow environments. The previous section showed that the shape of the turbulence velocity spectra from moored ADVs is consistent with Kolmogorov’s theory of locally isotropic turbulence, which has been observed consistently in turbulence measurements for decades (Kolmogorov 1941; Grant et al. 1962; McMillan et al. 2016). In particular, we observed an isotropic subrange—an $f^{-5/3}$ spectral slope and equal amplitude spectra between components—that is driven by anisotropic turbulence at longer timescales (Figures 8, 9, 10). This finding is interpreted as the first indication that the measurement systems presented are capable of accurately resolving turbulence. The degree to which uncorrected spectra were corrected toward this theoretical and observationally confirmed shape is interpreted as a measure of the improvement of the spectral estimates by motion correction.

Figure 12 presents a time series of the mean velocity (A) and several turbulence statistics that were measured during the June 2014 TTM deployment. This figure shows the evolution of the flow through Admiralty Inlet during 1.5 tidal cycles. The tke (B), Reynold’s stresses (C), dissipation, and one component of turbulence production (D) grow and strengthen with ebb or flood then subside during slack tide. This component of turbulence production is:

$$P_{uz} = \frac{\partial \bar{u}}{\partial z} \overline{uw} \quad . \quad (4)$$

Where $\partial \bar{u} / \partial z$ is computed from the two ADVs on the TTM. The highest values of ε and P_{uz} occur at the peak of the ebb or flood, which is in agreement with other measurements in tidal channels. The agreement of the magnitude of P_{uz} with ε at those times suggests a local production-dissipation

balance that is often observed in tidally forced channels (Trowbridge et al. 1999; Stacey et al. 1999b; McMillan et al. 2016). At other times, the value of P_{uz} is insufficient to balance ε or is negative.

Inspection of the negative P_{uz} values reveals that most of them are caused by a reversed sign of \overline{uw} rather than a reversed sign of $\partial u / \partial z$ (i.e., when compared to the sign of u). This finding suggests that uncertainty in \overline{uw} may be contributing to discrepancies between P_{uz} and ε . Furthermore, considering the complex nature of the shoreline near this site (i.e., the headland), it is not surprising that P_{uz} does not balance ε perfectly. Other terms of the tke equation are likely to be important, such as other components of production, advection terms, or turbulent transport terms. The fact that these two terms are in near balance as often as they are is a strong indication that bottom boundary layer physics are important to the dynamics at this site.

Figure 13 compares individual values of P_{uz} with ε directly. Given the assumptions implicit in this comparison and the discussion above, the agreement between P_{uz} and ε is an encouraging result that suggests the turbulent boundary reaches the depth of these measurements (10 m) during the highest flow speeds. This result is further supported by a comparison of \bar{U} with ε (Figure 14). Here we see a $\varepsilon \propto \bar{U}^3$ dependence that is again suggestive of bottom boundary layer physics (Trowbridge 1992; Nash et al. 2009). At lower flow speeds, ε deviates from this relationship, which suggests that the boundary layer is no longer the dominant physical process at the depth of these measurements.

6. Conclusion

This work presents a methodology for measuring turbulence from moored ADV-IMUs and demonstrates that motion correction reduces mooring motion-contamination. Comparison of spectra of ADV head motion, $S\{\vec{u}_h\}$, to that of motion-corrected, $S\{\vec{u}\}$, and uncorrected spectra,

434 $S\{\vec{u}_m\}$, reveals that motion correction improves spectral estimates of moored ADV measurements.
 435 In particular, we found that motion-corrected spectra have spectral shapes that are similar to previ-
 436 ous measurements of tidal-channel turbulence and have a $f^{-5/3}$ spectral slope at high frequencies.
 437 This finding suggests that the motion-corrected spectra resolve the inertial subrange predicted by
 438 Kolmogorov’s theory of locally isotropic turbulence.

439 Motion correction reduces motion contamination for all platforms we presented but it does not
 440 necessarily remove it completely. This outcome seems to depend on the relative amplitude of
 441 platform motion compared to the underlying turbulence being measured. The most notable ex-
 442 ample of this is from the TTM, which has a large “swaying” peak at 0.1 Hz. Where this peak
 443 is very large—especially in the v component—it is not reduced to a level that is consistent with
 444 earlier measurements of tidal-channel turbulence—i.e., there is no smooth roll-off between the
 445 low-frequency energy-containing scales and the $f^{-5/3}$ inertial subrange.

446 This inconsistency indicates that turbulence measurements from moored, motion-corrected IMU
 447 ADVs must be interpreted with care. An inspection of spectra presented here suggests that exclud-
 448 ing spectral regions where $S\{\vec{u}_h\}/S\{\vec{u}\} > 3$ removes persistent-motion contamination peaks while
 449 still preserving spectral regions where motion correction is effective. Using this criteria, it is then
 450 possible to produce spectral fits that exclude persistent-motion contamination, and provide reliable
 451 estimates of turbulence quantities of interest (e.g., ε and tke).

452 We’ve also shown that motion correction reduces motion contamination in cross spectra. This
 453 finding is important because it suggests that moored IMU-ADV measurements may be used to
 454 produce reliable estimates of Reynolds stresses. We utilized these stress estimates and vertical
 455 shear estimates, both from the TTM, to estimate P_{uz} .

456 Finally, we have shown that ε estimates based on motion-corrected spectra scale with the U^3 , and
 457 balance P_{uz} estimates during ebb and flood. Together, these results indicate that bottom boundary

458 layer physics are a dominant process at this site, and that the boundary layer reaches the height
459 of the IMU ADVs (10 m) during ebb and flood. The degree of agreement between P_{uz} and ε also
460 serves as an indicator of the self-consistency of moored IMU-ADV turbulence measurements.

461 *Acknowledgments.* Many thanks to Joe Talbert, Alex DeKlerk, Captain Andy Reay-Ellers, Jen-
462 nifer Rinker, Maricarmen Guerra, and Eric Nelson in assisting with data collection. The authors
463 are also grateful to James VanZwieten, Matthew Egeland and Marshall Richmond for discussion
464 on the details of this work.

465 This work was supported by the U.S. Department of Energy under Contract No. DE-AC36-
466 08GO28308 with the National Renewable Energy Laboratory. Funding for the work was provided
467 by the DOE Office of Energy Efficiency and Renewable Energy, Wind and Water Power Technolo-
468 gies Office.

469 The U.S. Government retains and the publisher, by accepting the article for publication, ac-
470 knowledges that the U.S. Government retains a nonexclusive, paid-up, irrevocable, worldwide
471 license to publish or reproduce the published form of this work, or allow others to do so, for U.S.
472 Government purposes.

A1. Comparing StableMoor \vec{u}_{low} to IMU \vec{u}_{h}

To better understand the IMU’s signal-to-noise ratio, we compare the motion of the StableMoor buoy from the ADP bottom track measurements, \vec{u}_{BT} , to the IMU’s estimates of ADP motion. To do this, we compute the IMU’s estimate of ADP motion using equation (2), and replacing ℓ^* with the vector that points from the IMU to the ADP head. We then linearly interpolate the ADP measurements of \vec{u}_{BT} onto the times of the ADV-IMU measurements.

The coherence between these two signals is high and statistically significant over 1.5 decades—from 0.03 to 0.8 Hz (Priestley 1981). The v component has the highest coherence, 98%, because this is the direction that has the most motion (i.e., these estimates have a higher signal-to-noise ratio). The u and w components have a slightly lower coherence, 80% and 65%, respectively.

On the low-frequency side, our interpretation is that the signal-to-noise ratio of the IMU increases dramatically below 0.03 Hz, resulting in low coherence. On the high-frequency side, Doppler noise in the ADP measurements contaminates its estimates of motion, causing the decrease in coherence at 0.8 Hz. A comparison of the phase between these signals shows that there is no lag between the measurements (not shown).

These results help to inform the selection of zero-lag filters used to estimate \vec{u}_{low} from \vec{u}_{BT} . In particular, by selecting 0.2 Hz, we target the middle of the coherence peak between the two measurements. Furthermore, the rapid decrease in coherence below 0.03 Hz provides an objective measurement of the frequency at which IMU measured velocity becomes unreliable in the flow conditions we observed.

References

- Afgan, I., J. McNaughton, S. Rolfo, D. Apsley, T. Stallard, and P. Stansby, 2013: Turbulent flow and loading on a tidal stream turbine by les and rans. *International Journal of Heat and Fluid Flow*, **43**, 96–108.
- Alexander, S. R., and P. E. Hamlington, 2015: Analysis of turbulent bending moments in tidal current boundary layers. *Journal of Renewable and Sustainable Energy*, **7** (6), 063 118.
- Alford, M. H., 2010: Sustained, full-water-column observations of internal waves and mixing near mendocino escarpment. *Journal of Physical Oceanography*, **40** (12), 2643–2660, doi:10.1175/2010JPO4502.1.
- Axford, D., 1968: On the accuracy of wind measurements using an inertial platform in an aircraft, and an example of a measurement of the vertical mesostructure of the atmosphere. *Journal of Applied Meteorology*, **7** (4), 645–666.
- Bachmann, E. R., X. Yun, D. McKinney, R. B. McGhee, and M. J. Zyda, 2003: Design and implementation of MARG sensors for 3-DOF orientation measurement of rigid bodies. *International Conference on Robotics & Automation*, Taipei, Taiwan.
- Barshan, B., and H. F. Durrant-Whyte, 1995: Inertial navigation systems for mobile robots. *IEEE Transactions on Robotics and Automation*, **11** (3), 328–342.
- Bevly, D. M., 2004: Global positioning system (gps): A low-cost velocity sensor for correcting inertial sensor errors on ground vehicles. *Journal of dynamic systems, measurement, and control*, **126** (2), 255–264.

514 Cartwright, G. M., C. T. Friedrichs, P. J. Dickhudt, T. Gass, and F. H. Farmer, 2009: Using the
515 acoustic doppler velocimeter (adv) in the mudbed real-time observing system. *Marine Technol-
516 ogy for Our Future: Global and Local Challenges*.

517 Doherty, K., D. Frye, S. Liberatore, and J. Toole, 1999: A moored profiling instrument*. *Journal
518 of Atmospheric and Oceanic Technology*, **16 (11)**, 1816–1829.

519 Edson, J. B., A. A. Hinton, K. E. Prada, J. E. Hare, and C. W. Fairall, 1998: Direct covariance
520 flux estimates from mobile platforms at sea*. *Journal of Atmospheric and Oceanic Technology*,
521 **15 (2)**, 547–562, doi:10.1175/1520-0426(1998)015<0547:DCFEFM>2.0.CO;2.

522 Egeland, M. N., 2014: Spectral evaluation of motion compensated ADV systems for ocean turbu-
523 lence measurements. Ph.D. thesis, Florida Atlantic University.

524 Fer, I., and M. B. Paskyabi, 2014: Autonomous ocean turbulence measurements using shear probes
525 on a moored instrument. *Journal of Atmospheric and Oceanic Technology*, **31 (2)**, 474–490, doi:
526 10.1175/JTECH-D-13-00096.1.

527 Finlayson, D., 2005: Combined bathymetry and topography of the Puget Lowlands, Washington
528 state. URL <http://www.ocean.washington.edu/data/pugetsound/>.

529 Geyer, R. W., M. E. Scully, and D. K. Ralston, 2008: Quantifying vertical mixing in estuaries.
530 *Environmental Fluid Mechanics*, **8**, 495–509, doi:10.1007/s10652-008-9107-2.

531 Goodman, L., E. R. Levine, and R. G. Lueck, 2006: On measuring the terms of the turbulent
532 kinetic energy budget from an auv. *Journal of Atmospheric and Oceanic Technology*, **23 (7)**,
533 977–990, doi:10.1175/JTECH1889.1.

534 Grant, H. L., R. W. Stewart, and A. Moilliet, 1962: Turbulence spectra from a tidal channel.
535 *Journal of Fluid Mechanics*, **12**, 241–263.

536 Gulmammadov, F., 2009: Analysis, modeling and compensation of bias drift in mems inertial
 537 sensors. *Recent Advances in Space Technologies, 2009. RAST'09. 4th International Conference*
 538 *on*, IEEE, 591–596.

539 Gunawan, B., V. S. Neary, and J. Colby, 2014: Tidal energy site resource assessment in the East
 540 River tidal strait, near Roosevelt Island, New York, NY (USA). *Renewable Energy*, **71**, 509–
 541 517, doi:10.1016/j.renene.2014.06.002.

542 Hand, M. M., N. D. Kelley, and M. J. Balas, 2003: Identification of wind turbine response to
 543 turbulent inflow structures. Tech. Rep. NREL/CP-500-33465, National Renewable Energy Lab-
 544 oratory.

545 Harding, S., L. Kilcher, and J. Thomson, 2017: Turbulence measurements from compliant moor-
 546 ings - part 1: Motion characterization, in review.

547 Kelley, N. D., B. J. Jonkman, G. N. Scott, J. T. Bialasiewicz, and L. S. Redmond, 2005: The impact
 548 of coherent turbulence on wind turbine aeroelastic response and its simulation. *WindPower*,
 549 Denver, Colorado, NREL/CP-500-38074, may 15-18.

550 Kilcher, L., J. Thomson, J. Talbert, and A. DeKlerk, 2016: Measuring turbulence from moored
 551 acoustic Doppler velocimeters: A manual to quantifying inflow at tidal energy sites. 9 62979,
 552 National Renewable Energy Laboratory. URL www.nrel.gov/docs/fy16osti/62979.pdf.

553 Kim, S. C., C. T. Friedrichs, J. P.-Y. Maa, and L. D. Wright, 2000: Estimating bottom stress in
 554 tidal boundary layer from acoustic doppler velocimeter data. *Journal of Hydraulic Engineering*,
 555 399–406.

556 Kolmogorov, A. N., 1941: Dissipation of energy in the locally isotropic turbulence. *Dokl. Akad.*
 557 *Nauk SSSR*, **32** (1), 16–18, URL <http://www.jstor.org/stable/51981>.

558 Kraus, C., A. Lohrmann, and R. Cabrera, 1994: A new acoustic meter for measuring 3d laboratory
559 flows. *Journal of Hydraulic Engineering*, **120**, 406–412.

560 Lohrmann, A., R. Cabrera, G. Gelfenbaum, and J. Haines, 1995: Direct measurements of reynolds
561 stress with an acoustic doppler velocimeter. *Current Measurement, 1995., Proceedings of the*
562 *IEEE Fifth Working Conference on*, 205–210, doi:10.1109/CCM.1995.516175.

563 Lorke, A., 2007: Boundary mixing in the thermocline of a large lake. *Journal of Geophysical*
564 *Research: Oceans*, **112 (C9)**, n/a–n/a, doi:10.1029/2006JC004008, c09019.

565 Lueck, R. G., and D. Huang, 1999: Dissipation measurement with a moored instrument in a swift
566 tidal channel. *Journal of atmospheric and oceanic technology*, **16**, 1499–1505.

567 Lumley, J., and E. Terray, 1983: Kinematics of turbulence convected by a random wave field.
568 *Journal of Physical Oceanography*, **13 (11)**, 2000–2007.

569 Marins, J. L., X. Yun, E. R. Bachmann, R. B. McGhee, and M. J. Zyda, 2001: An extended Kalman
570 filter for quaternion-based orientation estimation using MARG sensors. *Internation cconference*
571 *on intelligent robots and systems*.

572 McCaffrey, K., B. Fox-Kemper, P. E. Hamlington, and J. Thomson, 2015: Characterization of
573 turbulence anisotropy, coherence, and intermittency at a prospective tidal energy site: Observa-
574 tional data analysis. *Renewable Energy*, **76**, 441–453.

575 McMillan, J. M., A. E. Hay, R. G. Lueck, and F. Wolk, 2016: Rates of dissipation of turbulent
576 kinetic energy in a high reynolds number tidal channel. *Journal of Atmospheric and Oceanic*
577 *Technology*, **33 (4)**, 817–837, doi:10.1175/JTECH-D-15-0167.1.

578 MicroStrain, I., 2010: Technical note: Coning and sculling. Tech. Rep. I0019, MicroStrain. URL
579 http://files.microstrain.com/TN-I0019_3DM-GX3-25__Coning_And_Sculling.pdf.

580 MicroStrain, I., 2012: *3DM-GX3-15,-25 MIP Data Communications Protocol*. URL [http:](http://files.microstrain.com/3DM-GX3-15-25-MIP-Data-Communications-Protocol.pdf)
581 [//files.microstrain.com/3DM-GX3-15-25-MIP-Data-Communications-Protocol.pdf](http://files.microstrain.com/3DM-GX3-15-25-MIP-Data-Communications-Protocol.pdf), retrieved
582 January 2014.

583 Miller, S. D., T. S. Hristov, J. B. Edson, and C. A. Friehe, 2008: Platform motion effects on
584 measurements of turbulence and air-sea exchange over the open ocean. *Journal of Atmospheric*
585 *and Oceanic Technology*, **25 (9)**, 1683–1694, doi:10.1175/2008JTECHO547.1.

586 Morison, J. R., J. W. Johnson, and S. A. Schaaf, 1950: The force exerted by surface waves on
587 piles. *Journal of Petroleum Technology*, **2 (05)**, 149–154.

588 Moum, J., and J. Nash, 2009: Mixing measurements on an equatorial ocean mooring. *Journal of*
589 *Atmospheric and Oceanic Technology*, **26 (2)**, 317–336.

590 Mücke, T., D. Kleinhans, and J. Peinke, 2011: Atmospheric turbulence and its influence on the
591 alternating loads on wind turbines. *Wind Energy*, **14**, 301–316.

592 Nash, J. D., L. F. Kilcher, and J. N. Moum, 2009: Structure and composition of a strongly
593 stratified, tidally pulsed river plume. *Journal of Geophysical Research*, **114**, C00B12, doi:
594 10.1029/2008JC005036.

595 Nash, J. D., E. Kunze, J. M. Toole, and R. W. Schmitt, 2004: Internal tide reflection and turbulent
596 mixing on the continental slope. *Journal of Physical Oceanography*, **34 (5)**, 1117–1134, doi:
597 10.1175/1520-0485(2004)034<1117:ITRATM>2.0.CO;2.

598 Nortek, 2005: *Vector Current Meter User Manual*. Vangkroken 2, NO-1351 RUD, Norway, h ed.

599 Paskyabi, M. B., and I. Fer, 2013: Turbulence measurements in shallow water from a subsurface
600 moored moving platform. *Energy Procedia*, **35**, 307 – 316, doi:10.1016/j.egypro.2013.07.183.

601 Polagye, B., and J. Thomson, 2013: Tidal energy resource characterization: methodology and field
602 study in admiralty inlet, Puget Sound, WA (USA). *Proceedings of the Institution of Mechanical*
603 *Engineers, Part A: Journal of Power and Energy*, **227 (3)**, 352–367.

604 Priestley, M., 1981: *Spectral Analysis and Time Series*. Academic Press, London.

605 Rippeth, T. P., E. Williams, and J. H. Simpson, 2002: Reynolds stress and turbulent en-
606 ergy production in a tidal channel. *Journal of Physical Oceanography*, **32**, 1242–1251, doi:
607 10.1175/1520-0485(2002)032\$(<1242:RSATEP\$>\$2.0.CO;2.

608 Sreenivasan, K. R., 1995: On the universality of the Kolmogorov constant. *Physics of Fluids*, **7**,
609 2778–2784.

610 Stacey, M. T., S. G. Monismith, and J. R. Burau, 1999a: Measurements of reynolds stress
611 profiles in unstratified tidal flow. *J. Geophys. Res.*, **104 (C5)**, 10 933–10 949, doi:10.1029/
612 1998JC900095.

613 Stacey, M. T., S. G. Monismith, and J. R. Burau, 1999b: Observations of turbulence in a partially
614 stratified estuary. *Journal of Physical Oceanography*, **29**, 1950–1970.

615 Thomson, J., B. Polagye, V. Durgesh, and M. Richmond, 2012: Measurements of turbulence at
616 two tidal energy sites in Puget Sound, WA. *Journal of Oceanic Engineering*, **37 (3)**, 363–374,
617 doi:10.1109/JOE.2012.2191656.

618 Trowbridge, J. H., 1992: A simple description of the deepening and structure of a stably stratified
619 flow driven by a surface stress. *Journal of Geophysical Research*, **97**, 15 529–15 543.

620 Trowbridge, J. H., W. R. Geyer, M. M. Bowen, and A. J. I. Williams, 1999: Near-bottom turbu-
621 lence measurements in a partially mixed estuary: turbulent energy balance, velocity structure
622 and along-channel momentum balance. *Journal of Physical Oceanography*, **29**, 3056–3072.

623 van der Walt, S., S. C. Colbert, and G. Varoquaux, 2011: The numpy array: A structure for efficient
624 numerical computation. *Computing in Science & Engineering*, **13**, 22–30, doi:10.1109/MCSE.
625 2011.37.

626 VanZwieten, J. H., M. N. Egeland, K. D. von Ellenrieder, J. W. Lovenbury, and L. Kilcher, 2015:
627 Experimental evaluation of motion compensated adv measurements for in-stream hydrokinetic
628 applications. *Current, Waves and Turbulence Measurement (CWTM), 2015 IEEE/OES Eleventh*,
629 1–8, doi:10.1109/CWTM.2015.7098119.

630 Voulgaris, G., and J. H. Trowbridge, 1998: Evaluation of the acoustic doppler velocimeter (adv)
631 for turbulence measurements. *Journal of Atmospheric and Oceanic technology*, **15**, 272–289.

632 Walter, R. K., N. J. Nidzieko, and S. G. Monismith, 2011: Similarity scaling of turbulence spectra
633 and cospectra in a shallow tidal flow. *Journal of Geophysical Research: Oceans*, **116** (C10).

634 Wiles, P. J., T. P. Rippeth, J. H. Simpson, and P. J. Hendricks, 2006: A novel technique for
635 measuring the rate of turbulent dissipation in the marine environment. *Geophysical Research*
636 *Letters*, **33**, 21 608.

637 Winkel, D., M. Gregg, and T. Sanford, 1996: Resolving oceanic shear and velocity with the multi-
638 scale profiler. *Journal of Atmospheric and Oceanic Technology*, **13** (5), 1046–1072.

639 Wyngaard, J. C., L. Rockwell, and C. A. Friehe, 1985: Errors in the measurement of turbulence
640 upstream of an axisymmetric body. *Journal of Atmospheric and Oceanic Technology*, **2** (4),
641 605–614.

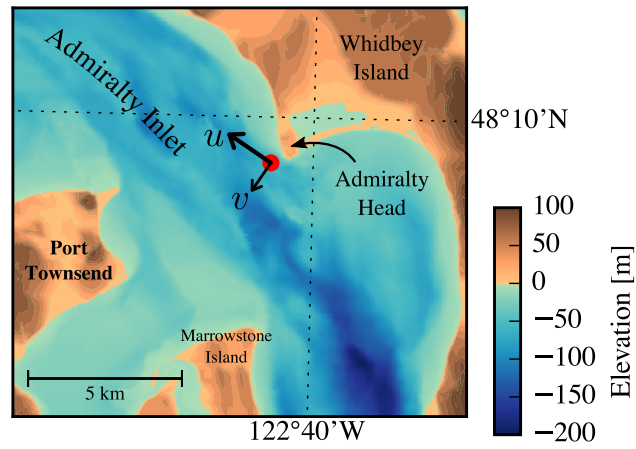
642 Zhang, Y., K. Streitlien, J. G. Bellingham, and A. B. Baggeroer, 2001: Acoustic doppler ve-
643 locimeter flow measurement from an autonomous underwater vehicle with applications to deep

644 ocean convection. *Journal of Atmospheric and Oceanic Technology*, **18** (12), 2038–2051, doi:
645 10.1175/1520-0426(2001)018<2038:ADVFMF>2.0.CO;2.

LIST OF FIGURES

646	Fig. 1.	Bathymetry of Admiralty Inlet near Port Townsend, Washington, U.S.A. (Finlayson 2005). The red dot indicates the location of all measurements. The positive u direction is the direction of ebb flow (thick arrow originating from red dot), and positive v is away from Admiralty Head (smaller arrow).	34
647	Fig. 2.	Schematic diagram of the TTM; not to scale.	35
648	Fig. 3.	TTM components on the deck of the R/V Jack Robertson. The TTM includes two ADVs, with pressure cases mounted on opposite sides of the fin. The anchor stack includes a pop-up buoy for retrieval. The green arrow indicates the vector from the IMU to the ADV head (face of the transmit transducer).	36
649	Fig. 4.	Top: Alex DeKlerk checks to ensure that the StableMoor buoy is properly fastened to its anchor; the RDI workhorse ADCP can be seen in the rear instrument bay. A bridle is draped across the top of the buoy for deployment and recovery, and a small marker buoy fastened to the tail is useful during recovery. Bottom: a close-up of the StableMoor with the ADV head and the top of its pressure case. The green arrow indicates the vector from the IMU to the ADV head.	37
650	Fig. 5.	The turbulence platform showing details of the ADV head and pressure case configuration. The green arrow indicates the vector from the IMU to the ADV head. The head cable was taped out of the way beneath the sounding weight tail fins shortly after taking this photo.	38
651	Fig. 6.	Spectra of \vec{u}_ω (yellow) and \vec{u}_a signals from the Microstrain IMU sitting on a motionless table. The \vec{u}_a signals are unfiltered (black), and high-pass filtered at 30 s (magenta), 10 s (blue), 5 s (green). Vertical dotted lines indicate the filter frequency. The black horizontal dotted line indicates the noise level of a Nortek Vector ADV configured to measure $\pm 4\text{m/s}$. The shaded region indicates the range of spectra presented herein ($0.002 < \text{tke} < 0.03 \text{ m}^2/\text{s}^2$, $1\text{e-}5 < \varepsilon < 5\text{e-}4 \text{ W/kg}$).	39
652	Fig. 7.	Time series of tidal velocity at Admiralty Head from TTM measurements (black), and an acoustic Doppler profiler (red). The profiler measurements—taken at the same depth as the ADV on the TTM—were contaminated by acoustic reflection from the strongback fin when it was inline with one of the profiler’s beams. Note that the vertical scale on the three axes vary by more than an order of magnitude; the small ticks in A and B are equivalent to the ticks in C.	40
653	Fig. 8.	Turbulence spectra from the June 2014 TTM deployment. Each column is for a range of streamwise velocity magnitudes (indicated at top). The rows are for each component of velocity (indicated to the lower right of the right column). The uncorrected spectra are in black and the corrected spectra are blue, and the spectra of ADV head motion, \vec{u}_h , is red (also indicated in the legend). The vertical red dotted line indicates the filter frequency applied to the IMU accelerometers when estimating \vec{u}_h ; below this frequency $S\{\vec{u}_h\}$ is plotted as a dashed line. Diagonal black dotted lines indicate a $f^{-5/3}$ slope. The number of spectral ensembles, N , in each column is indicated in the top row.	41
654	Fig. 9.	Turbulence spectra from the StableMoor buoy. The axes layout and annotations are identical to Figure 8, except that $S\{\vec{u}_h\}$ is plotted as a solid line at all frequencies because it is measured at all frequencies.	42

688	Fig. 10.	Turbulence spectra from the turbulence torpedo during a 35-minute period when the mean velocity was 1.3 m/s. Annotations and line colors are identical to Figure 8.	43
689			
690	Fig. 11.	The real part of the cross-spectral density between velocity components measured by the TTM. The upper row is the u - v cross-spectral density, the middle row is the u - w cross-spectral density, and the bottom row is the v - w cross-spectral density. The columns are for different ranges of the stream-wise mean velocity magnitude (indicated above the top row). The blue line is the cross spectrum between components of motion-corrected velocity, the red line is the cross spectrum between components of head-motion, and the black line is the cross spectrum between components of uncorrected velocity. The light blue shading indicates one standard deviation of the C for the motion-corrected cross-spectral density. N is the number of spectral ensembles in each column. The number in the lower-right corner of each panel is the motion-corrected Reynold's stress (integral of the blue line) in units of $1\text{e-}4 \text{ m}^2\text{s}^{-2}$	44
691			
692			
693			
694			
695			
696			
697			
698			
699			
700			
701	Fig. 12.	Time series of mean velocities (A), turbulence energy and its components (B), Reynold's stresses (C), and turbulence dissipation rate (D) measured by the TTM during the June 2014 deployment. Shading indicates periods of ebb ($\bar{u} > 1.0$, grey) and flood ($\bar{u} < -1.0$, lighter grey).	45
702			
703			
704			
705	Fig. 13.	$P_{u\bar{z}}$ vs. ϵ during the June 2014 TTM deployment for values of $ u > 1$ m/s. Values of negative production are indicated as open circles.	46
706			
707	Fig. 14.	A log-log plot of ϵ versus \bar{U} for the June 2014 TTM (diamonds) and May 2015 StableMoor (dots) deployments, during ebb (left) and flood (right). Black points are 5-minute averages. Green dots are mean values within speed bins of 0.2 m s^{-1} width that have at least 10 points (50 minutes of data); their vertical bars are 95% bootstrap confidence intervals. The blue line shows a U^3 slope, wherein the proportionality constant (blue box) is calculated by taking the log-space mean of ϵ/U^3	47
708			
709			
710			
711			
712			
713	Fig. 15.	Coherence between IMU-measured motion of StableMoor buoy and ADP bottom-track velocity for $1.0 < \bar{U} < 1.5$. The horizontal dotted line indicates the 95% confidence level for the 102 spectral windows in this estimate.	48
714			
715			



716 FIG. 1. Bathymetry of Admiralty Inlet near Port Townsend, Washington, U.S.A. (Finlayson 2005). The red
 717 dot indicates the location of all measurements. The positive u direction is the direction of ebb flow (thick arrow
 718 originating from red dot), and positive v is away from Admiralty Head (smaller arrow).

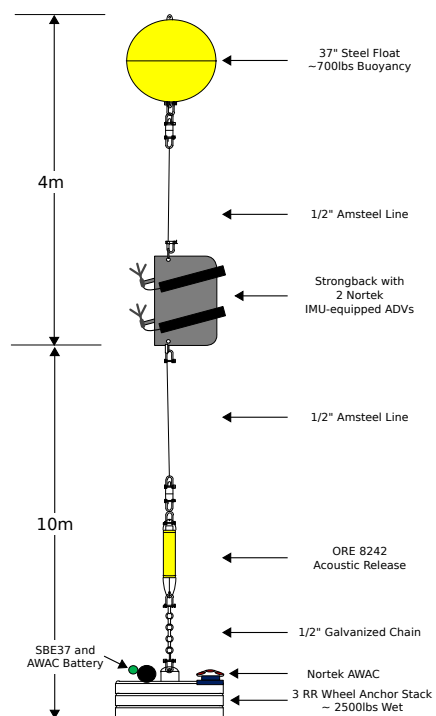


FIG. 2. Schematic diagram of the TTM; not to scale.



719 FIG. 3. TTM components on the deck of the R/V Jack Robertson. The TTM includes two ADVs, with
 720 pressure cases mounted on opposite sides of the fin. The anchor stack includes a pop-up buoy for retrieval. The
 721 green arrow indicates the vector from the IMU to the ADV head (face of the transmit transducer).



722 FIG. 4. Top: Alex DeKlerk checks to ensure that the StableMoor buoy is properly fastened to its anchor; the
 723 RDI workhorse ADCP can be seen in the rear instrument bay. A bridle is draped across the top of the buoy
 724 for deployment and recovery, and a small marker buoy fastened to the tail is useful during recovery. Bottom: a
 725 close-up of the StableMoor with the ADV head and the top of its pressure case. The green arrow indicates the
 726 vector from the IMU to the ADV head.



727 FIG. 5. The turbulence platform showing details of the ADV head and pressure case configuration. The green
728 arrow indicates the vector from the IMU to the ADV head. The head cable was taped out of the way beneath the
729 sounding weight tail fins shortly after taking this photo.

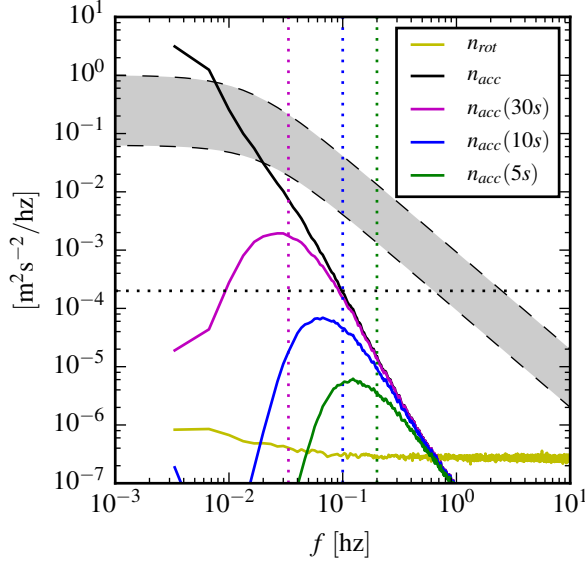
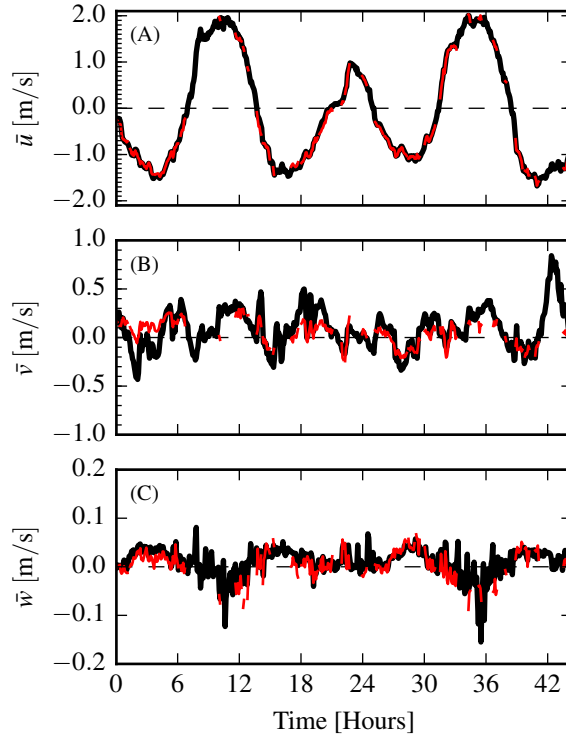


FIG. 6. Spectra of \vec{u}_ω (yellow) and \vec{u}_a signals from the Microstrain IMU sitting on a motionless table. The \vec{u}_a signals are unfiltered (black), and high-pass filtered at 30 s (magenta), 10 s (blue), 5 s (green). Vertical dotted lines indicate the filter frequency. The black horizontal dotted line indicates the noise level of a Nortek Vector ADV configured to measure $\pm 4\text{m/s}$. The shaded region indicates the range of spectra presented herein ($0.002 < \text{tke} < 0.03 \text{ m}^2/\text{s}^2$, $1\text{e-}5 < \varepsilon < 5\text{e-}4 \text{ W/kg}$).



735 FIG. 7. Time series of tidal velocity at Admiralty Head from TTM measurements (black), and an acoustic
 736 Doppler profiler (red). The profiler measurements—taken at the same depth as the ADV on the TTM—were
 737 contaminated by acoustic reflection from the strongback fin when it was inline with one of the profiler’s beams.
 738 Note that the vertical scale on the three axes vary by more than an order of magnitude; the small ticks in A and
 739 B are equivalent to the ticks in C.

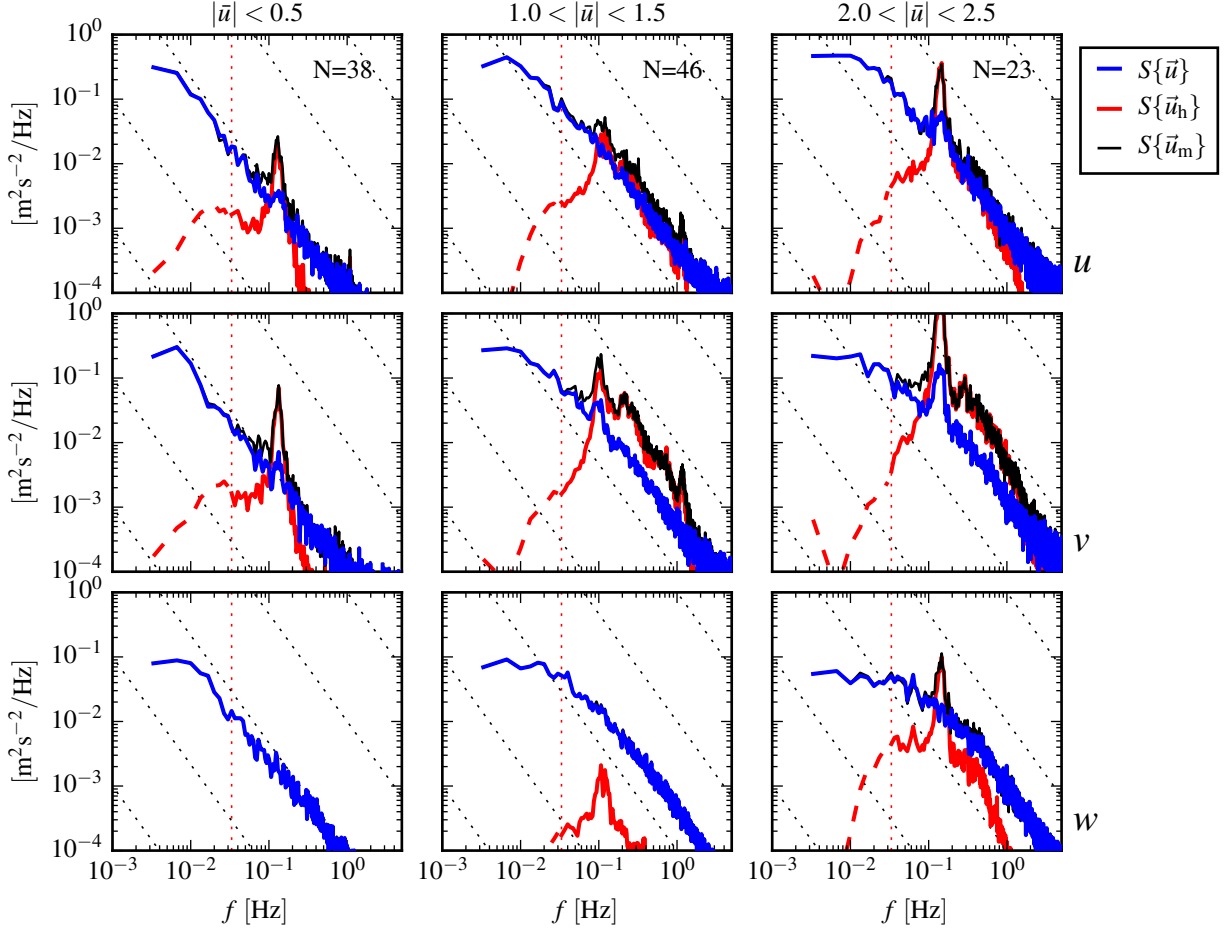


FIG. 8. Turbulence spectra from the June 2014 TTM deployment. Each column is for a range of streamwise velocity magnitudes (indicated at top). The rows are for each component of velocity (indicated to the lower right of the right column). The uncorrected spectra are in black and the corrected spectra are blue, and the spectra of ADV head motion, \vec{u}_h , is red (also indicated in the legend). The vertical red dotted line indicates the filter frequency applied to the IMU accelerometers when estimating \vec{u}_h ; below this frequency $S\{\vec{u}_h\}$ is plotted as a dashed line. Diagonal black dotted lines indicate a $f^{-5/3}$ slope. The number of spectral ensembles, N , in each column is indicated in the top row.

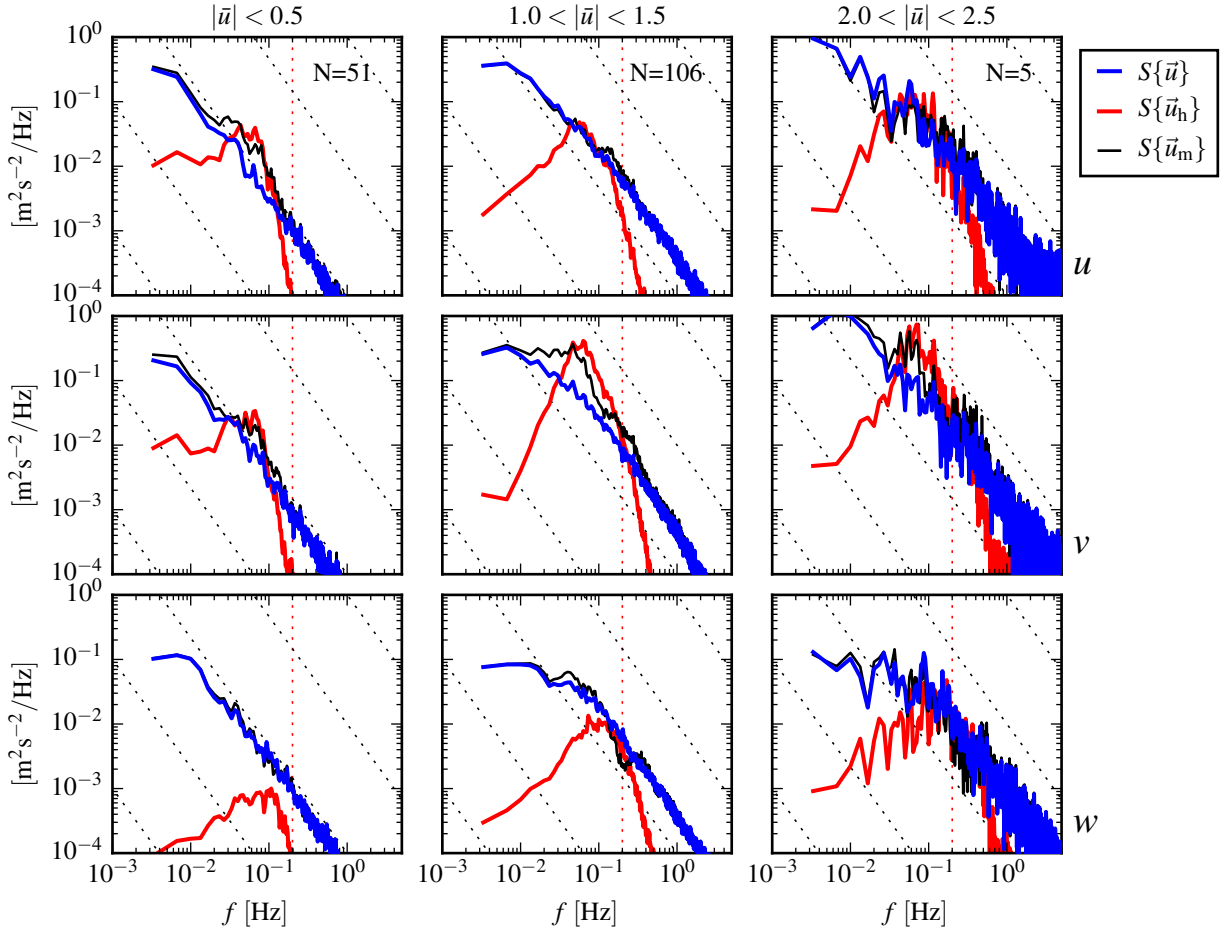


FIG. 9. Turbulence spectra from the StableMoor buoy. The axes layout and annotations are identical to Figure 8, except that $S\{\vec{u}_h\}$ is plotted as a solid line at all frequencies because it is measured at all frequencies.

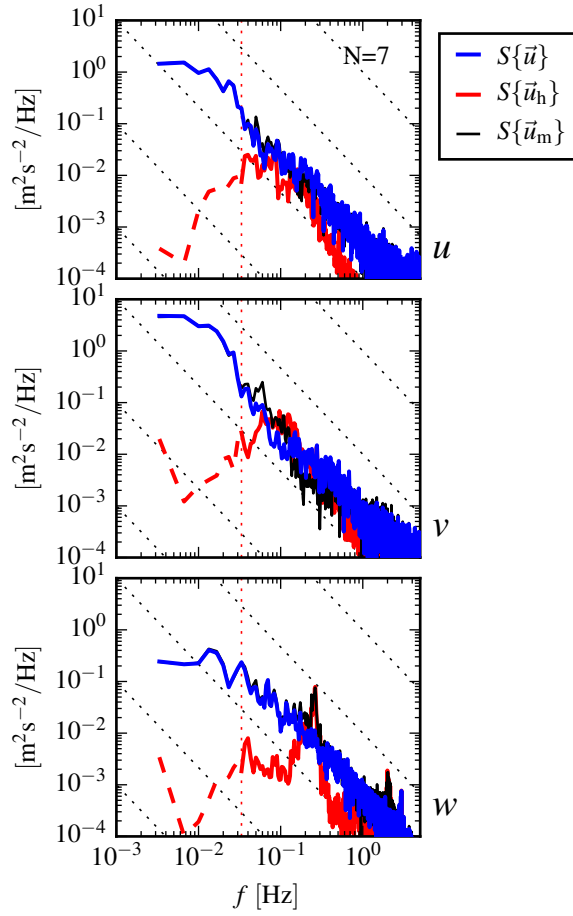


FIG. 10. Turbulence spectra from the turbulence torpedo during a 35-minute period when the mean velocity was 1.3 m/s. Annotations and line colors are identical to Figure 8.

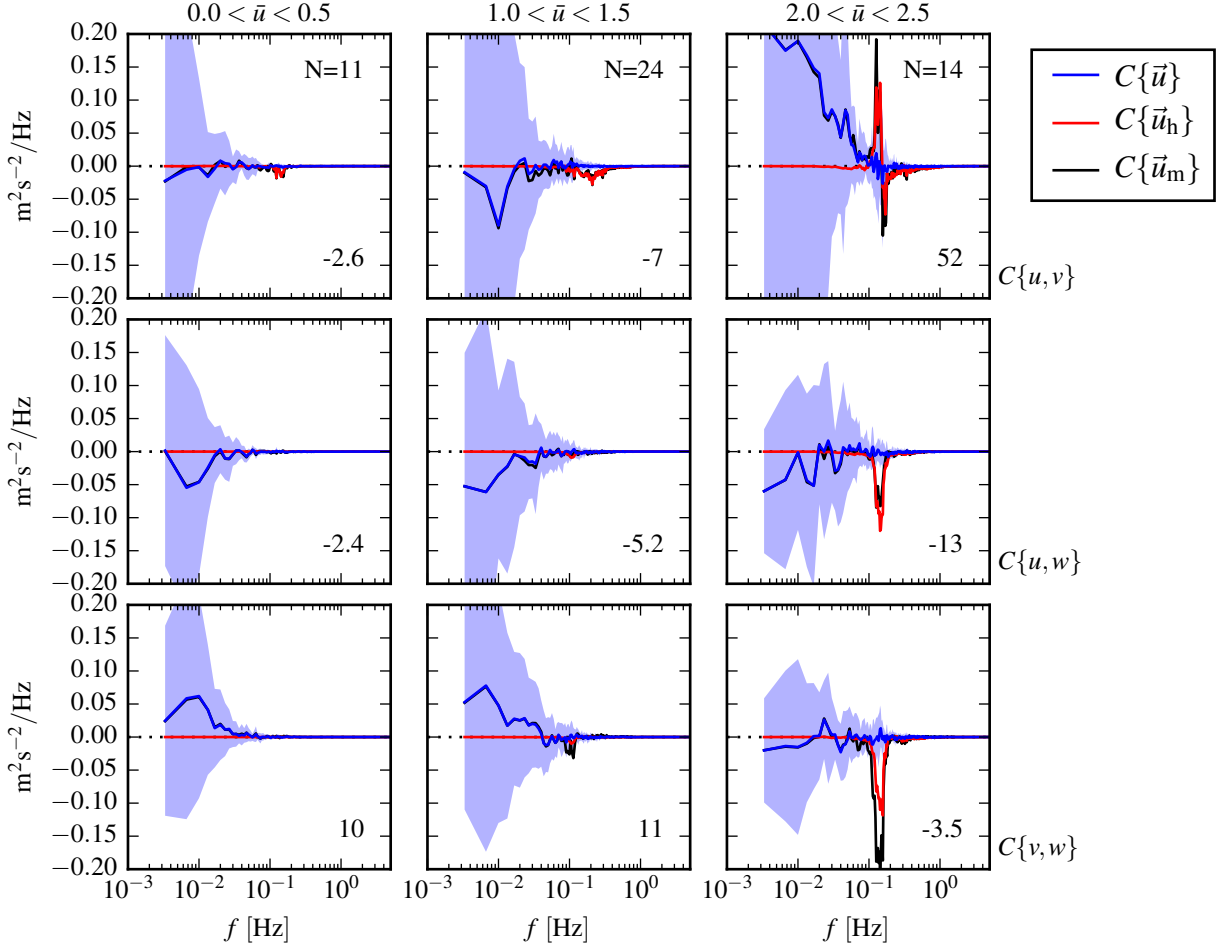


FIG. 11. The real part of the cross-spectral density between velocity components measured by the TTM. The upper row is the u - v cross-spectral density, the middle row is the u - w cross-spectral density, and the bottom row is the v - w cross-spectral density. The columns are for different ranges of the stream-wise mean velocity magnitude (indicated above the top row). The blue line is the cross spectrum between components of motion-corrected velocity, the red line is the cross spectrum between components of head-motion, and the black line is the cross spectrum between components of uncorrected velocity. The light blue shading indicates one standard deviation of the C for the motion-corrected cross-spectral density. N is the number of spectral ensembles in each column. The number in the lower-right corner of each panel is the motion-corrected Reynold's stress (integral of the blue line) in units of $1\text{e-}4 \text{ m}^2\text{s}^{-2}$.

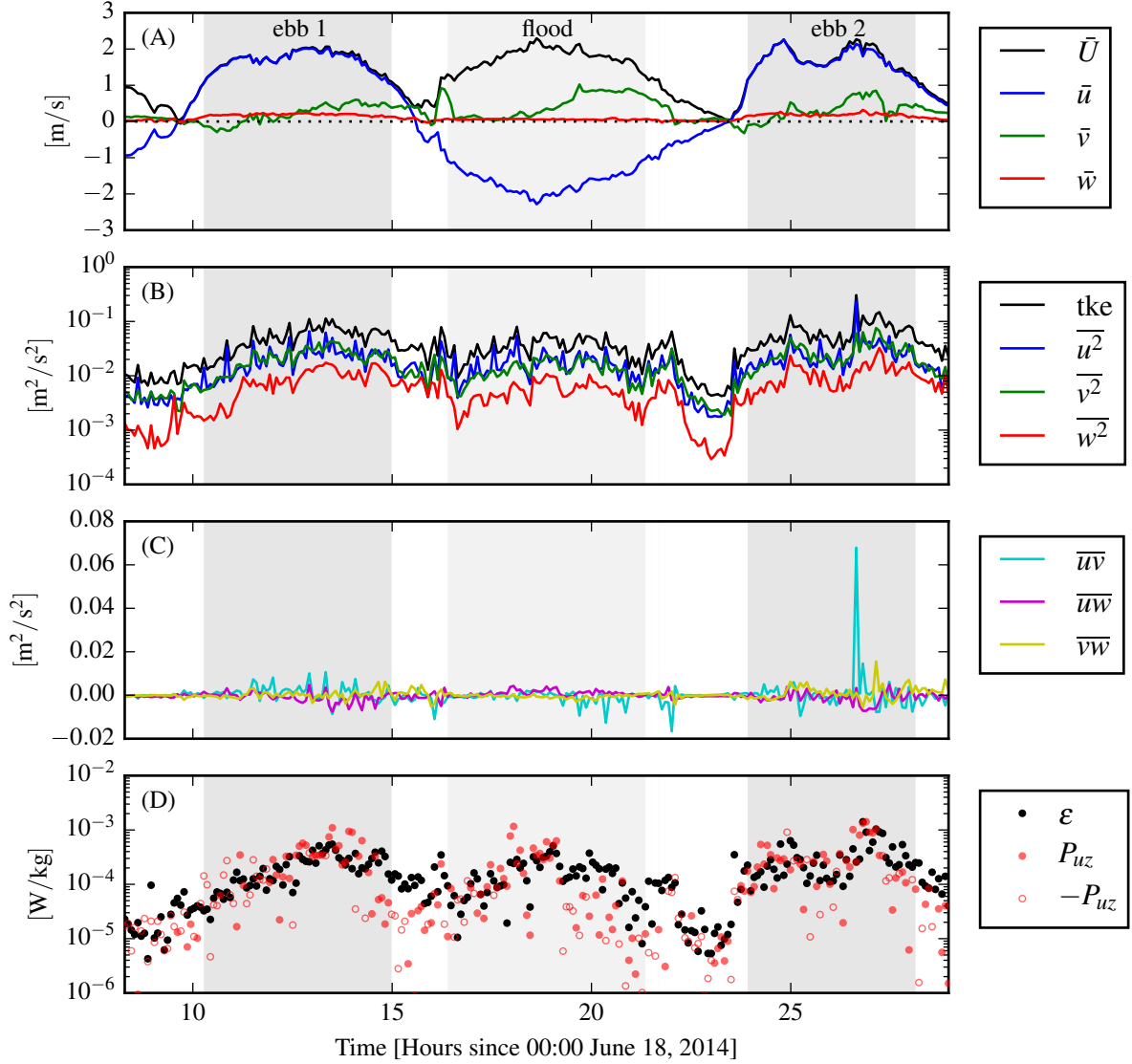


FIG. 12. Time series of mean velocities (A), turbulence energy and its components (B), Reynold's stresses (C), and turbulence dissipation rate (D) measured by the TTM during the June 2014 deployment. Shading indicates periods of ebb ($\bar{u} > 1.0$, grey) and flood ($\bar{u} < -1.0$, lighter grey).

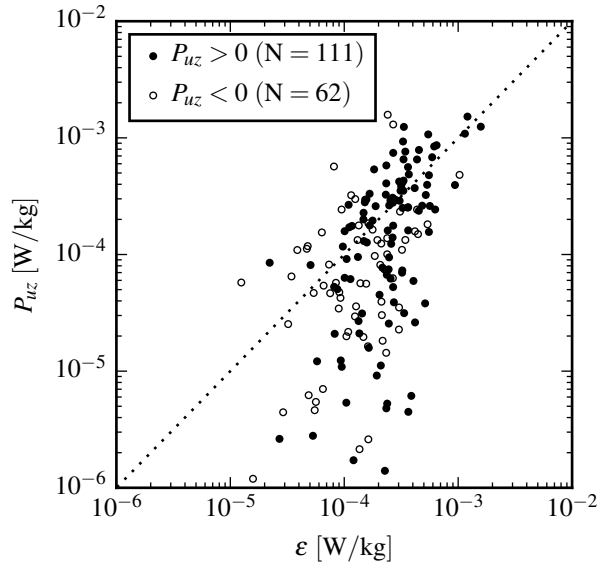


FIG. 13. P_{uz} vs. ε during the June 2014 TTM deployment for values of $|u| > 1$ m/s. Values of negative production are indicated as open circles.

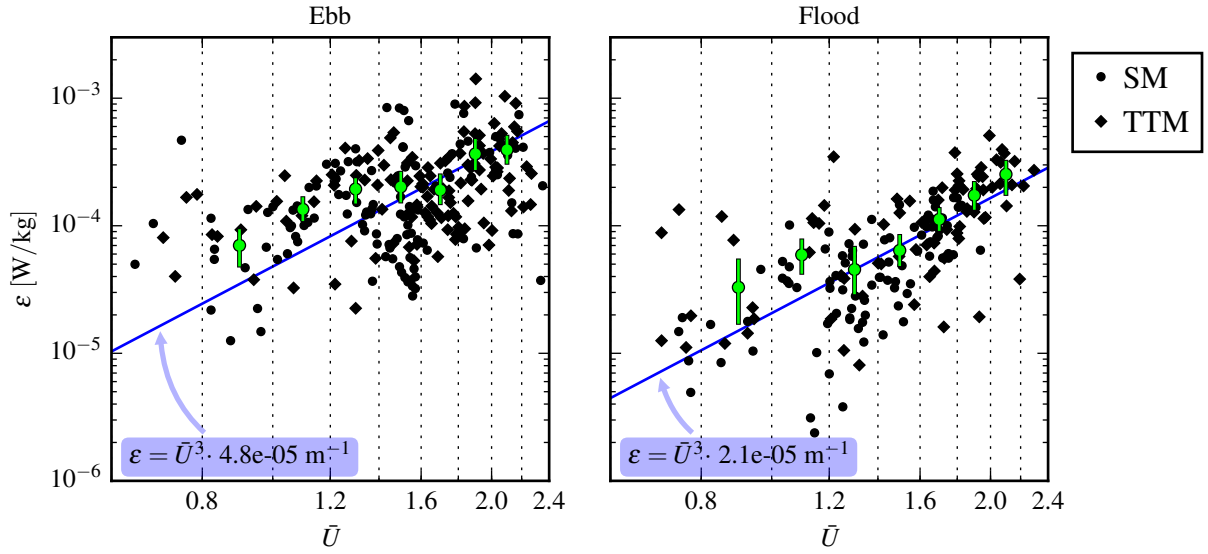


FIG. 14. A log-log plot of ε versus \bar{U} for the June 2014 TTM (diamonds) and May 2015 StableMoor (dots) deployments, during ebb (left) and flood (right). Black points are 5-minute averages. Green dots are mean values within speed bins of 0.2 m s^{-1} width that have at least 10 points (50 minutes of data); their vertical bars are 95% bootstrap confidence intervals. The blue line shows a U^3 slope, wherein the proportionality constant (blue box) is calculated by taking the log-space mean of ε/U^3 .

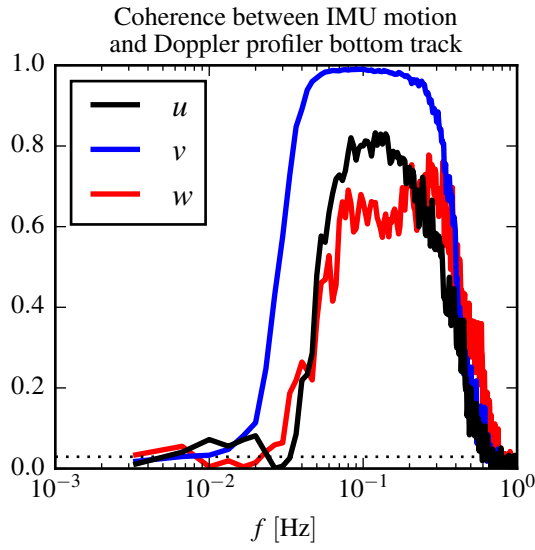


FIG. 15. Coherence between IMU-measured motion of StableMoor buoy and ADP bottom-track velocity for $1.0 < \bar{U} < 1.5$. The horizontal dotted line indicates the 95% confidence level for the 102 spectral windows in this estimate.